Quantum molecular dynamics of warm dense iron and a five-phase equation of state

Travis Sjostrom and Scott Crockett
Theoretical Division, Los Alamos National Laboratory, Los Alamos, New Mexico 87545, USA

(Received 24 October 2017; published 24 May 2018)

Through quantum molecular dynamics (QMD), utilizing both Kohn-Sham (orbital-based) and orbital-free density functional theory, we calculate the equation of state of warm dense iron in the density range 7–30 g/cm^3 and temperatures from 1 to 100 eV. A critical examination of the iron pseudopotential is made, from which we find a significant improvement at high pressure to the previous QMD calculations of Wang *et al.* [Phys. Rev. E **89**, 023101 (2014)]. Our results also significantly extend the ranges of density and temperature that were attempted in that prior work. We calculate the shock Hugoniot and find very good agreement with experimental results to pressures over 20 TPa. These results are then incorporated with previous studies to generate a five-phase equation of state for iron.

DOI: 10.1103/PhysRevE.97.053209

I. INTRODUCTION

Iron is among the most well-studied materials at ambient conditions as well as extreme pressure and temperature conditions. The case of iron in extreme conditions has been of primary interest as the essential component of the Earth's core, in both the liquid state and as a high temperature and pressure solid [1]. The need for understanding the thermodynamic properties of iron at much higher temperatures and pressures than at Earth's core conditions is exemplified by the cases of giant planet and exoplanet cores [2] as well as giant-impact simulations and theories of the Earth-Moon system formation [3]. Shock experiments have continued to press results to even higher pressures and temperatures [4,5]. There also exist many investigations from a theoretical perspective. One recent effort has been the *ab initio* examination of body-centered cubic (bcc) and hexagonal close-packed phase iron up to 1500 GPa and up to 1 eV through QMD, including calculations of the melt curve [6]. A later effort is the QMD study of fluid iron by Wang *et al.* [7]. For our work, while we sought to extend the range of results (in density and pressure) given by Wang *et al.* we found issues at high pressure in their method in terms of the pseudopotential usage.

In this paper, first we present our QMD results for the liquid regime of iron for wide ranging densities of 7 to 30 g/cm^3 and temperatures from 1 to 100 eV. We begin with a description of our QMD approach with special attention to the pseudopotential issue. Then we present and analyze our results for the liquid iron equation of state, including the shock Hugoniot. Second, based on these calculations and solid regime QMD calculations [6] as well as significant experimental results, we construct a five-phase equation of state (EOS) for iron, which is available in the Los Alamos National Laboratory SESAME equation of state database [8]. Previous wide-ranging multiphase EOS have been developed [9,10], as well as more recent examinations up to Earth core conditions [11]. Our EOS, however, is based on *ab initio* calculations at high pressures and temperatures, where experimental results are not available, as well as the most recent experimental results for a both wide ranging and highly accurate EOS.

II. QUANTUM MOLECULAR DYNAMICS

A. Methods

Kohn-Sham-based QMD simulations have become the gold standard for calculations of warm dense matter. The success lies in the accurate treatment of the quantum nature of the electrons, through the Mermin-Kohn-Sham density functional theory (DFT) [12], and the ionic, possibly strongly coupled, motion, through the molecular dynamics of the classically treated ions. Yet this approach suffers a prohibitive scaling issue with increasing temperature due the increasing number of Kohn-Sham orbitals that must be calculated. An alternative approach without such an issue is provided by orbital-free DFT; the issue here, however, is the accuracy of the necessary approximation for the kinetic (plus entropic) free-energy functional. While the simple Thomas-Fermi approximation has been used successfully at very high temperatures, there is significant loss of accuracy at lower temperatures [13]. Recently we have developed and applied an approach correcting the Thomas-Fermi approximation through an additional density gradient term which is determined by matching Kohn-Sham calculations at lower temperatures [14]. This then allows for extension through very high temperatures. It is this approach we use in this work, for which the development and implementation details may be found in Ref. [14].

In the current case of iron, we have performed Kohn-Sham DFT QMD simulations with unit cells containing 54 to 60 atoms from 1 to 5 eV in temperature using the Quantum-Espresso code [15]. Each simulation included at least 4000 time steps after equilibration and a time step of 0.5–0.25 fs was used. We used the Perdew-Burke-Ernzerhof exchange-correlation functional [16] and for densities less than 17.5 g/cm^3 we used a projector augmented wave (PAW) [17] 8-electron pseudopotential, while for greater densities we used a 16-electron pseudopotential. The Andersen thermostat was used for the NVT (constant number of atoms, volume, and temperature) simulations.

The use of a pseudopotential is critical to making the QMD simulations computationally tractable. Two keys are first there

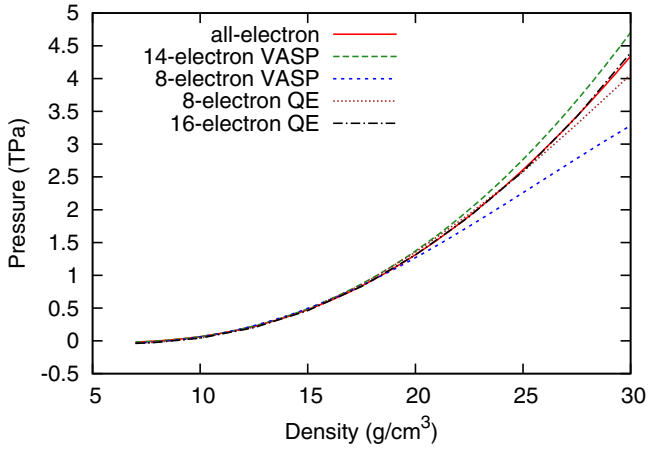

FIG. 1. Zero temperature calculation for bcc iron. Overlap of the cutoff radius, and the lack of sufficient number of valence states, causes the VASP 8-electron pseudopotential to be valid only for densities less than 18 g/cm^3.

is a cutoff radius below which the ion Coulomb potential is regularized, and second core electrons are frozen and do not participate in the calculation. Semicore orbitals have lower energy levels than typical valence electrons, but as pressure and temperature increase they may begin to interact and need to be included in the calculation. We validated our pseudopotentials in part by examining bcc phase, $T = 0$ pseudopotential calculations in comparison with all-electron calculations, which an accurate pseudopotential should reproduce. As can be seen in Fig. 1 the only pseudopotential that reproduces the all-electron calculations is the 16-electron pseudopotential used in the quantum-espresso (QE) code. The 8-electron Vienna *ab initio* simulation package (VASP) pseudopotential [18] is valid to no more than 18 g/cm^3. While validating pseudopotentials is always important, in the case of warm dense matter the issues as demonstrated here can be pronounced, and having sufficiently small cutoff radii as well as inclusion of enough semicore orbitals is critical.

Using the approach described in Ref. [14] we performed gradient corrected orbital-free DFT calculations. Here the free energy is given by standard Thomas-Fermi approximation plus a gradient correction coefficient of varying strength given by λ,

$$F_s[n] = F_{TF}[n,T] + \lambda \int \frac{|\nabla n(\mathbf{r})|^2}{8n(\mathbf{r})} d\mathbf{r}. \quad (1)$$

To determine λ, for each density we found the value which reproduced the Kohn-Sham calculated pressures at $T = 5$ eV. It is then fixed at all higher temperatures for that density. At 5 eV, the Kohn-Sham calculations are already getting computationally expensive; however, after performing the pressure match at 5 eV, we found the slope in pressure with respect to temperature increase to match between the two methods, which lends confidence to using the orbital-free approach at that low of temperature. For iron λ was found to increase from 0.240 at 7 g/cm^3 to 0.296 at 30 g/cm^3. For the orbital-free simulations 60 atoms were included in the unit cell, and 6000 time steps were completed after 2000 time steps of equilibration. The time steps varied with temperature from 0.25 to 0.0125 fs, and the

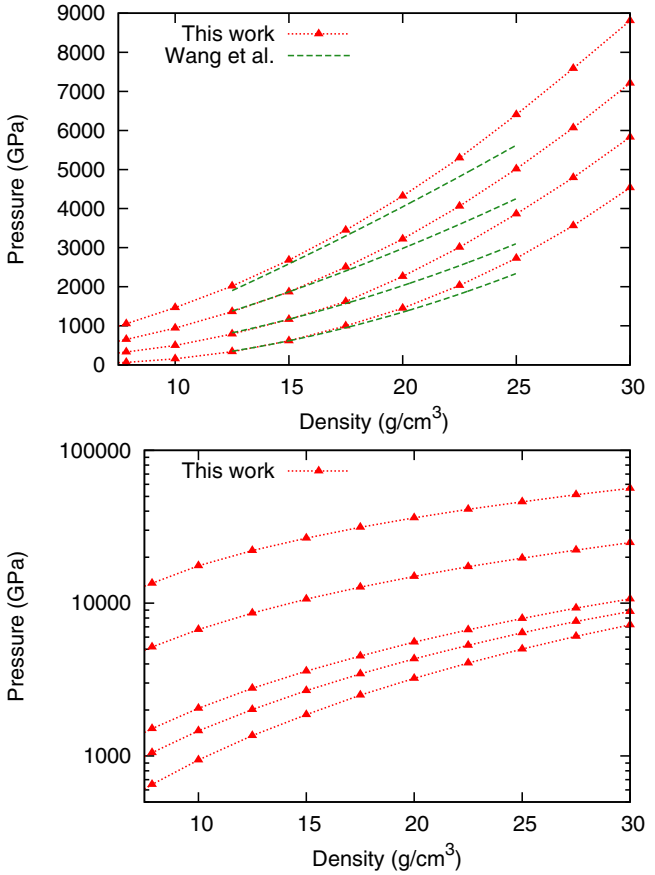

FIG. 2. Upper panel: Pressure isotherms at $T = 1, 5, 10, 15$ eV from the current work compared with the fit from Wang *et al.* [7]. The pseudopotential used in Ref. [7] is insufficient at the higher densities it is employed at and those results deviate from ours starting below 17.5 g/cm^3. Lower panel: High temperature pressure isotherms at $T = 10, 15, 20, 50, 100$ eV. Curves at 10 eV and above are from the orbital-free QMD.

simulations were thermostatted via the isokinetic ensemble. All-electron local pseudopotentials were employed using the method given in Ref. [13] and a cutoff radius of 0.6 times the Wigner-Seitz radius. For aluminum this means all 13 electrons per atom are included in the density being calculated and above the cutoff radius the ion potential is $-13/r$, while below it is regularized going to a finite value at $r = 0$.

B. Results

In Fig. 2 pressure isotherms from our QMD calculations are plotted from both moderate and high temperatures. First in the upper panel we compare with the fit results of Wang *et al.*'s QMD calculations, over their stated range of applicability which is from 12.5 to 25 g/cm^3 and 1 to 15 eV. In Ref. [7] they state their calculations are made using the VASP code and PAW formalism, though they do not state what is the exchange-correlation functional or which pseudopotential is used. Comparing Figs. 1 and 2, it seems clear they used the standard iron PBE PAW with eight electrons beyond its region of applicability. Whether it is in fact PBE is not the issue, this order of discrepancy cannot be accounted for by

exchange-correlation. Rather the issue is the pseudopotential they used has too large of a cutoff radius and does not include enough semicore orbitals to accurately describe the higher densities it is applied to. Thus, the results of Wang *et al.* should be regarded as low in pressure except for the region up to twofold compression (∼16 g/cm^3). Between temperatures of 10 and 15 eV lower energy states, which are frozen in the Wang pseudopotential, begin to ionize as well, though this only a few percent at 15 eV and so does not have much effect on the pressure.

Our results, however, span from 7 to 30 g/cm^3 and 1 to 100 eV. For the Kohn-Sham QMD (up to 5 eV) we transition from an 8-electron pseudopotential to a 16-electron pseudopotential at 17.5 g/cm^3, at which density full calculations from both pseudpotentials were done and found to be in agreement for the pressure. The results above 5 eV are from the orbital-free QMD. There is if course a shift in the energy from the change in pseudopotential for both the local pseudopotentials used in the orbital-free calculations and the 8 to 16 electron PAW pseudpotentials, which has been accounted for in the following calculation of the Hugoniot.

In Fig. 3 we present our QMD results for the shock Hugoniot of iron, which is calculated via the Rankine-Hugoniot equations:

$$E - E_0 = (P + P_0)(V_0 - V)/2, \tag{2}$$

$$(P - P_0) = \rho_0 U_s u_p, \tag{3}$$

$$\rho = \rho_0 U_s/(U_s - u_p). \tag{4}$$

Here E, P, V, and ρ are the internal energy, pressure, volume, and mass density, respectively, and the 0 subscript denotes the initial state. While U_s and u_p are the shock and particle velocities. From our QMD calculations smooth fits along individual isochores or isotherms are used to solve Eq. (2). All of our Hugoniot results are in the liquid regime between 12.5 and 30 g/cm^3, and are shown in the upper panel of Fig. 3. In the lower panel we focus on the Hugoniot up to twofold compression. Here we show for reference the experimental completion of the shock melt (that is when the system is completely liquefied) at 270 GPa [4]. We find that pressure at $\rho = 12.50$ g/cm^3 and $T = 6025$ K, whereas the values calculated from experiment are 12.51 g/cm^3 and 6300 K [4]. Over the entire range we find good agreement with the collection of experimental results [19–41], which are shown sans error bars for clarity. Also shown in both panels is the SESAME 2140 table results [8], which show softening with respect to ours results and experimental results from the shock melt onward.

We have fit our Hugoniot results in terms of U_s and u_p through Eqs. (3) and (4), where $\rho_0 = 7.874$ g/cm^3. The fit uses the exponential form as given in Ref. [42],

$$U_s = a + bu_p + cu_p e^{-du_p}, \tag{5}$$

with U_s and u_p in km/s and parameters $a = 3.7885$, $b = 1.25524$, $c = 0.518106$, and $d = 0.0866344$. Though the parameters were determined by fitting only to our liquid regime results, the fit comes into agreement with the SESAME 2140 curve below 11 g/cm^3 and also agrees with the solid regime experiments. Our fit curve is shown in both panels of Fig. 3.

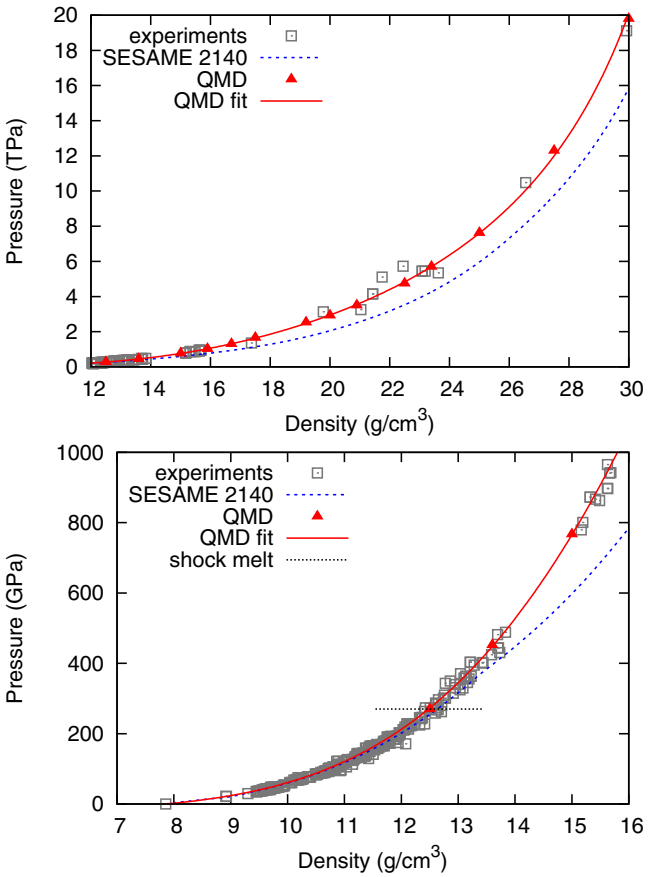

FIG. 3. Shock Hugoniot of iron with $\rho_0 = 7.874$ g/cm^3. Our QMD results (triangles) are shown along with our $U_s(u_p)$ fit, and are seen to be in good agreement with available experimental results [19–41]. The SESAME 2140 Hugoniot begins to soften relative to our results and experiment from just below the shock melt completion at about 12.5 g/cm^3 and 270 GPa. The uncertainty in the experiments is mostly conveyed by the scatter in the data, except at the highest densities, above 24 g/cm^3, where the uncertainty in density is 1 g/cm^3 or more.

As a matter of course we also have the QMD temperatures along the Hugoniot, which are plotted up to 2 TPa in Fig. 4. Additionally we have fit the Hugoniot temperature in terms of the Hugoniot pressure up to 40 eV and 20 TPa by a polynomial fit as given in Table I, which is also shown in Fig. 4. The

TABLE I. Fit parameters, c_i, for the temperature along the Hugoniot according to $T_H = \sum_{i=0}^{4} c_i P_H^i$, with T_H in eV and P_H in GPa.

	$0 < P_H < 2500$	$2500 < P_H < 20\,000$
c0	0	0.550988
c1	1.24182×10^{-3}	2.93777×10^{-3}
c2	2.80723×10^{-6}	-7.75673×10^{-8}
c3	-1.31703×10^{-9}	1.31292×10^{-12}
c4	1.88449×10^{-13}	0

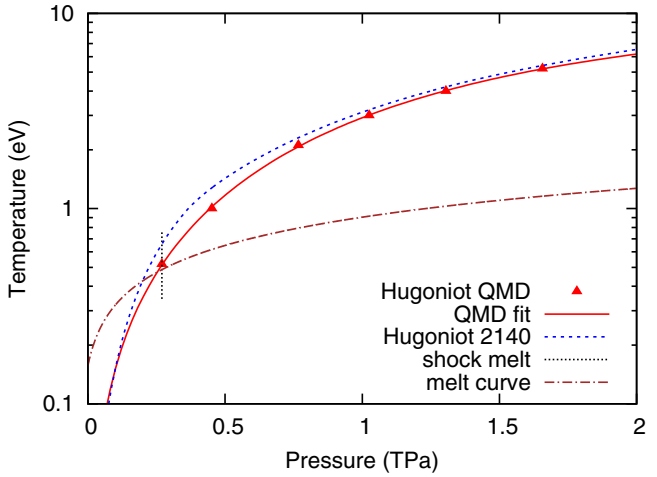

FIG. 4. Temperature along the iron shock Hugoniot. Our calculated Hugoniot temperatures and current fit, are shown along with the SESAME 2140 temperatures and the melt curve of Bouchet *et al.* [6]. Also marked is the experimental shock melt completion at 270 GPa.

QMD based melt curve of Bouchet *et al.* [6] is plotted here for reference, and it is seen that the intersection of our temperature curve is very near the completion of the shock melt at 270 GPa. The intersection is in fact slightly lower at 253 GPa. Taking into account that the initialization of melt from the bcc phase is at 243 GPa [4], this is completely reasonable since the two-phase method used by Bouchet *et al.* to calculate the melt curve should be expected to, on average, yield the midpoint of the transition region which would be about 256 GPa. We note here that our $U_s(u_p)$ and Hugoniot temperature fits are accurate over the liquid region, and though we have extrapolated through the solid region, this is at best an approximate average over the features that should be found due to the iron phase transitions.

III. MULTIPHASE EQUATION OF STATE

A. Construction

The multiphase iron equation of state (EOS) consists of the liquid phase, the ambient magnetic alpha phase, the high pressure epsilon (hpc) phases, as well as the higher temperature gamma and delta phases which lie primarily between the alpha phase and melt. Our EOS follows the standard SESAME modeling which separates the Helmholtz free energy into three components,

$$F = F_0(\rho) + F_i(\rho,T) + F_e(\rho,T), \tag{6}$$

where ρ is the material density, T is the temperature, F_0 is the zero temperature energy curve, and F_i and F_e are the thermal contributions of the ions and electrons, respectively. Each phase is determined separately and then the phase boundaries are determined by examining the Gibbs free energy. Each component is based on models with a set of physical parameters to be determined. The reasoning for the use of models is that the EOS must cover a very broad range of densities, from tiny fractions to tens or hundreds times ambient solid densities, and temperature from zero to tens of millions K. These model parameters may be known to some degree from experiment, for example ambient pressure measurement of thermal expansion and heat capacities, or isothermal compression from diamond anvil experiments. However, for the warm dense matter regime we have little data, which is essentially only shock Hugoniot data. This is where the QMD is valuable in that as shown in Sec. II, it reproduces the the experimental shock data accurately, validating the method, and further providing significant data off-Hugoniot where there is lack of experiments.

TABLE II. Parameters from the cold curve models for iron

Phase	Alpha	Epsilon	Gamma	Delta	Liquid
ρ_0 (g/cc)	7.98	8.38	8.15	8.10	7.85
B (GPa)	175	185	175	175	165
dB/dP	4.8	4.75	4.8	4.8	3.65
C_1	—	—	—	—	120
ρ_{LJ} (g/cc)	7.480	7.874	7.401	7.401	7.401
f_{LJ}	1.2	1.0	0.65	0.65	0.65
E_{coh} (kcal/mol)	54	99.4	54	54	54
ρ_{TF} (g/cc)	23.62	10.63	23.62	23.62	10.23
E_{shift} (MJ/kg)	0.0	-0.055	0.05	0.125	0.42

For all of our phases the cold curve is give by a Birch-Murnaghan finite-strain form, which connects to a Lennard-Jones model below ambient density (7.874 g/cm^3) and a Thomas-Fermi-Dirac approximation at high compression. The finite strain equation is of the form

$$F_0(\rho) = \left\{ \frac{9}{2}\left[\eta^{2/3} + \left(\frac{dB}{dP}\bigg|_{\rho_0} - 4\right)\eta^3\right] + \sum_{j=1}^{N_{\text{terms}}} \frac{C_i \eta^{j+3}}{(i+3)!} \right\} \frac{B|_{\rho_0}}{\rho_0} + E_{\text{shift}}. \tag{7}$$

Here $\eta = 1/2[(\rho/\rho_0)^{2/3} - 1]$, and the input parameters are the bulk modulus B and its pressure derivative dB/dP at the reference density ρ_0 as well as the expansion coefficients C_i and the overall energy shift E_{shift}. The transition the to the Lennard-Jones model at low density is given by [43]

$$F_0(\rho < \rho_{LJ}) = f_1\rho_2^f - f_3\rho^{f_{LJ}} + E_{coh}, \tag{8}$$

where ρ_{LJ} is the lower compression cutoff matchpoint, f_{LJ} is an input exponent, and E_{coh} is the input cohesive energy. f_1, f_2, and f_3 are then found by requiring that the energy, pressure, and $dP/d\rho$ are continuous at ρ_{LJ}.

Last, at high compression the cold curve is given by

$$F_0(\rho > \rho_{TF}) = [E_{TF}(\rho) - E_{TF}(\rho_{TF})]y(\rho) + \Delta E, \tag{9}$$

with

$$y(\rho) = 1 + \frac{b_1}{\rho} + \frac{b_2}{\rho^{4/3}}. \tag{10}$$

Here E_{TF} is the zero temperature result of an average atom Thomas-Fermi-Dirac calculation. The parameters ΔE, b_1, and b_2 are again found by matching the energy, pressure and $dP/d\rho$ at the input upper compression matchpoint ρ_{TF}. The cold curve model parameters for all phases are presented in Table II.

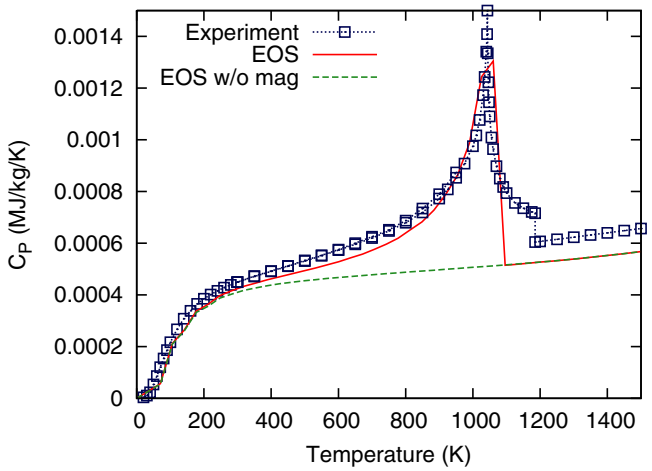

FIG. 5. Total heat capacity of iron from experiment [49,50] is shown with comparison to the alpha phase EOS with and without the $F_{\rm mag}$ contribution.

The thermal electronic term is from a set of Thomas-Fermi-Dirac (TFD) average atom calculations [44,45]. Here every temperature-density grid point in the SESAME table is calculated and the difference between the energy at finite temperature and the zero temperature results at the same density is the electronic contribution, $F_e(\rho,T)$. This is the same for all phases, with the exception of the alpha phase. The alpha phase is magnetic and we must add a contribution for this to the TFD free energy result. This contribution has been found experimentally [46–48] to be pressure independent and fit to the form

$$F_{\rm mag} = a^3 b\left[\left(1-\frac{T}{a^2}\right)\ln\left(\frac{1+\sqrt{T/a^2}}{1-\sqrt{T/a^2}}\right) - 2\sqrt{\frac{T}{a^2}} + \frac{4}{3}\left(\frac{T}{a^2}\right)^3\right] \tag{11}$$

for temperatures up to the Curie temperature $T_C = 1043$ K, with parameters $a^2 = 1135$ K and $a^3 b = 4680$ J/mol. After adding $F_{\rm mag}$ to F_e for the alpha phase we are able to reproduce to experimental total heat capacity, as shown in Fig. 5. With just the TFD energy no peak for the heat capacity is produced for the alpha phase.

For the solid phases the ion thermal contributions are given by a Debye model. Here the free energy is given by

$$F_i(\rho,T) = \frac{R}{M}\left[\frac{9}{8}\theta + 3T\ln\left(1-e^{-\theta/T}\right) - T\,D(\theta/T)\right], \tag{12}$$

where

$$D(x) = \frac{3}{x^3}\int_0^x \frac{y^3}{e^y-1}dy \tag{13}$$

is a Debye function for the energy, R is the ideal gas constant, M is the atomic weight (55.845), T is the temperature. Also θ is the Debye temperature which is dependent on the density through the Grüneisen parameter, γ, by the relation $\gamma = d\ln\theta/d\ln\rho$. We impose an analytic model for γ to determine

TABLE III. Parameters from the ion thermal model for iron

Phase	Alpha	Epsilon	Gamma	Delta	Liquid
$\theta_{\rm ref}$	470	380	275	256	—
$\gamma_{\rm ref}$	1.95	1.8	2.35	2.55	2.35
$\gamma_{'R}$	−1.95	−1.0	−1.35	−0.75	−1.0
$\gamma_{'L}$	−1.95	−1.0	−1.35	−0.75	−1.0
γ_0	20	1.0	1.0	1.0	1.0
γ_∞	0.6667	0.6667	0.6667	0.6667	0.5

θ. The model is given by the following equations:

$$\gamma(\rho \geqslant \rho_{\rm ref}) = \gamma_\infty + \frac{\rho_{\rm ref}}{\rho}(2\gamma_{\rm ref} - 2\gamma_\infty + \gamma'_R) + \left(\frac{\rho_{\rm ref}}{\rho}\right)^2(\gamma_\infty - \gamma_{\rm ref} - \gamma'_R), \tag{14}$$

$$\gamma(\rho < \rho_{\rm ref}) = \gamma_0 + \frac{\rho}{\rho_{\rm ref}}(2\gamma_{\rm ref} - 2\gamma_0 - \gamma'_L) + \left(\frac{\rho}{\rho_{\rm ref}}\right)^2(\gamma_0 - \gamma_{\rm ref} + \gamma'_L). \tag{15}$$

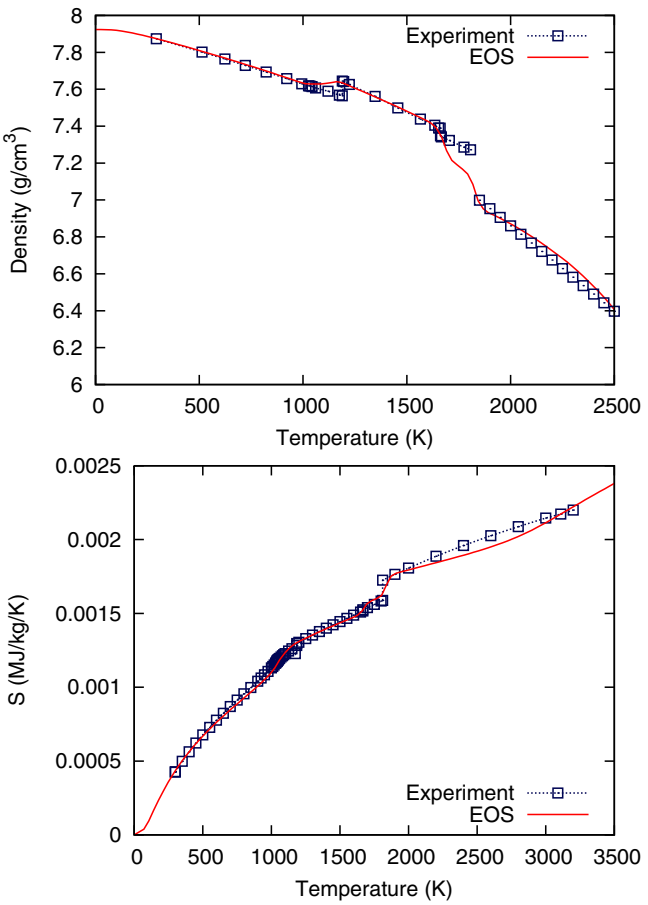

FIG. 6. Isobaric results for thermal expansion [52,53] and entropy [50] at 1 atm for iron. Transitions from alpha to gamma to delta to liquid for the EOS can be seen to be in good agreement with experiment.

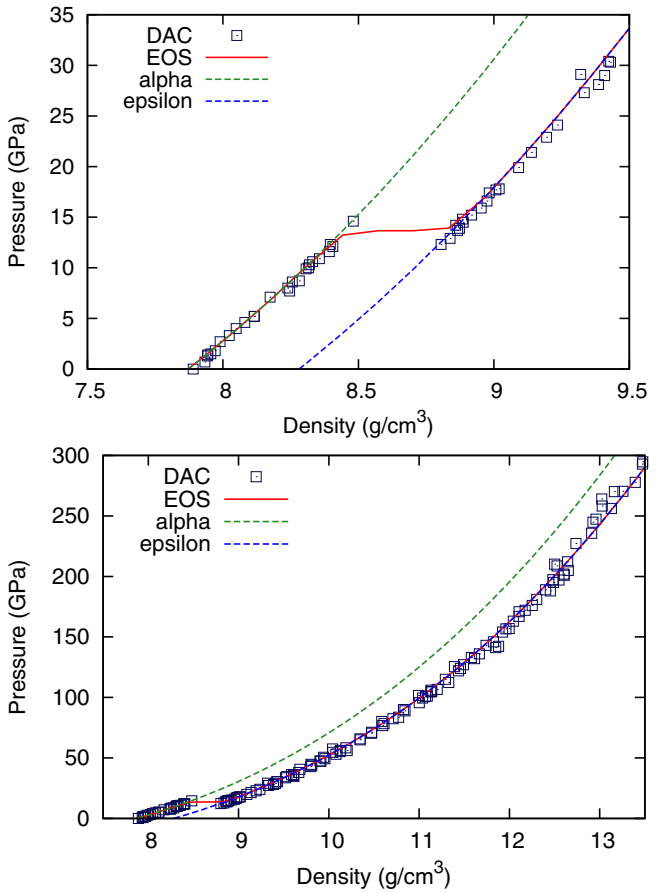

FIG. 7. Diamond anvil cell compression at 300 K, shown with the multiphase EOS 300 K isotherm (solid line) which transitions from alpha to epsilon phase at 13 GPa. The individual phases are shown with dashed lines.

Here γ_0 and γ_∞ are the values at $\rho = 0$ and $\rho = \infty$. γ'_L and γ'_R are the left and right logarithmic density derivatives of γ at ρ_{ref}. ρ_{ref} is the reference density (7.874 g/cm^3 in all cases) and γ_{ref} is the value of γ at that density. Additionally, θ_{ref}, the value of θ at the reference density, is specified to fix the constant of integration when solving for θ. The ion model parameter values are summarized in Table III.

For the liquid regime we use the model of Johnson, in particular version 2 from Ref. [51], which was found to reproduce the QMD isotherm data well. In general, this model interpolates from Debye-like at low temperatures to the ideal gas limit at very high temperatures. Here we use Johnson's suggested value for $a = 1.25/M^{5/3} = \theta^2/T_m\rho^{2/3}$, which relates the Debye and melt, T_m, temperatures in eV along with the density ρ, in g/cm^3. Additional parameters for the model are the initial melt temperature and density which we set as 290 K and 6.9 g/cm^3. The melt temperature parameter is not realistic, but was found as the best value for the model to match the QMD results. It should be noted the EOS melt temperature at 1 atm is 1800 K determined by Gibb's energy comparison between the phases. Last, the liquid model requires a Grüneisen model for which we use the same as for the solid phases, the parameters are given in Table III, note that θ_{ref} is determined within the model.

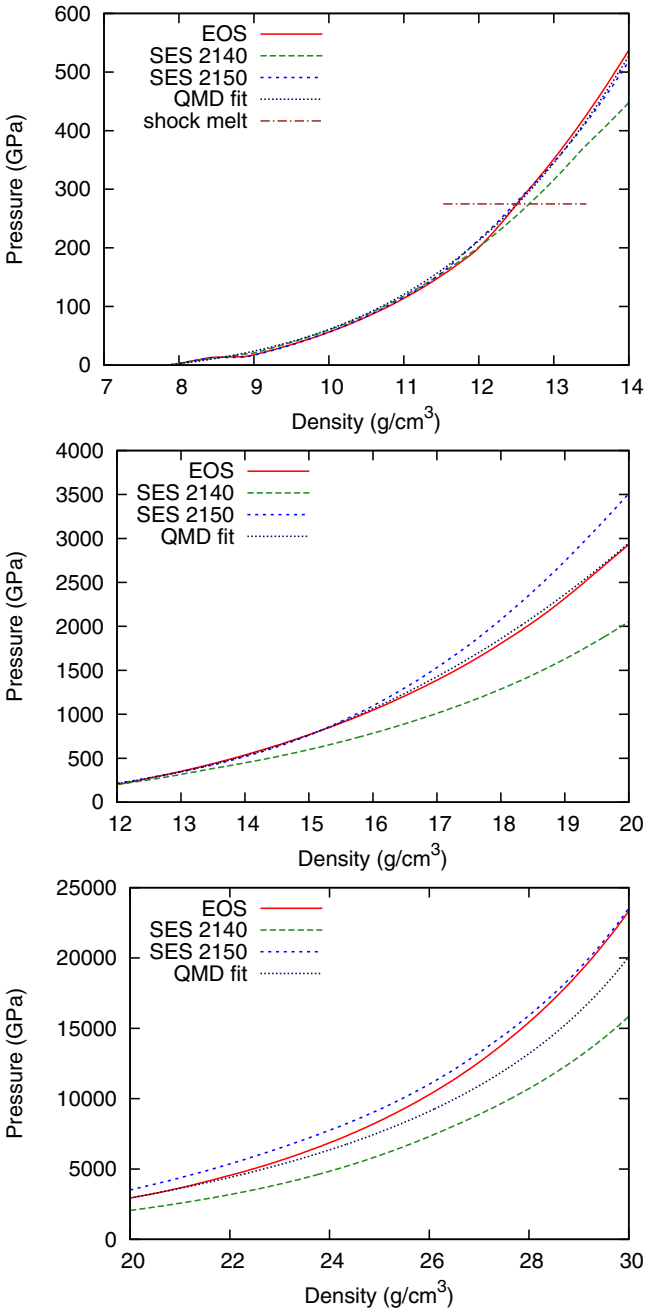

FIG. 8. Iron Hugoniot for $\rho_0 = 7.874$ g/cc. Here the current EOS and two previous EOSs are compared to the QMD fit. The current EOS gives the best agreement up to 50 Mbar, while the previous Kerley EOS (SES 2150) diverges at 10 Mbar.

B. Results

We first consider the ambient pressure isobaric results for the EOS. This encompasses the ambient temperature magnetic alpha phase, followed by two solid-solid phase transitions, first to gamma phase and then to delta phase as the temperature increases. Then at 1800 K the delta phase melts. The four phases are seen in Fig. 6 where both the thermal expansion, shown in terms of density versus pressure and the entropy are shown. The EOS is in very good agreement with the

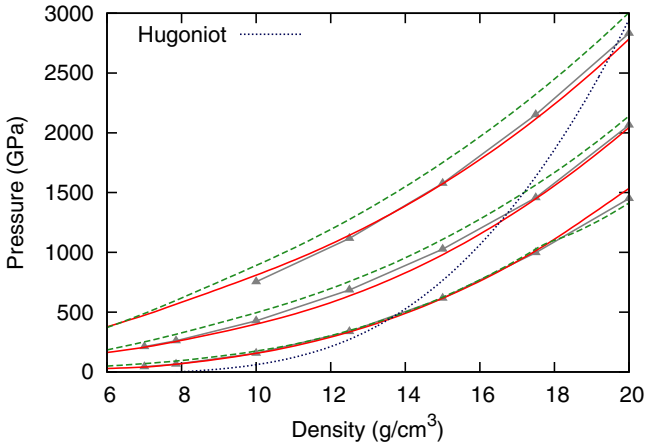

FIG. 9. Pressure isotherms from the EOS (solid lines) are in good agreement with QMD results (triangles) for $T = 1,4,8$ eV. The SESAME 2150 EOS (dashed line) isotherms are shown to be overly stiff with temperature and pressure increase. The Hugoniot path is also shown.

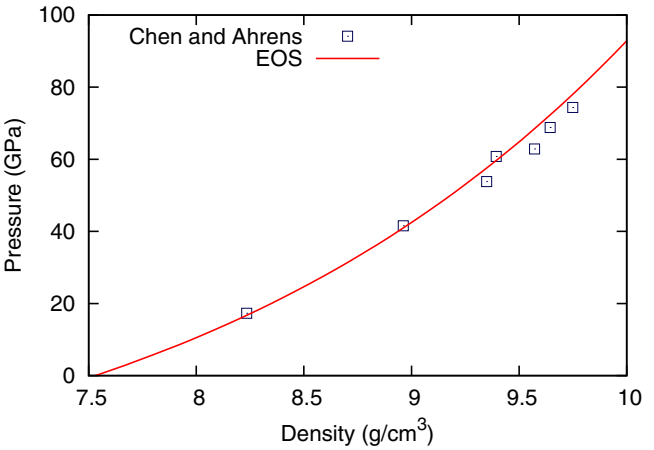

FIG. 10. Hugoniot for gamma iron shocked from ambient pressure and 1573 K.

experimental results as was shown previously for the specific heat, Fig. 5

Next we consider the isothermal compression at 300 K. Diamond anvil cell (DAC) data [54–56] is shown in Fig. 7 along with the EOS results. Here the individual alpha and epsilon phases are shown by dashed lines and the multiphase EOS is shown with the solid line transitioning from alpha to epsilon at about 13 GPa. Good agreement is seen with all data up to 300 GPa.

In Fig. 8 the Hugoniot from the current EOS is compared with QMD based $U_s(u_p)$ fit, which was shown above to be in good agreement with experiment. In addition we show the results from two previous SESAME EOSs 2140 and 2150 [9]. The SESAME 2140 EOS is soft compared to the QMD beginning at pressure below the shock melt, while the SESAME 2150 EOS is in good agreement up to 10 Mbar (1 Mbar = 100 GPa), where it stiffens by comparison. Our current EOS is in good agreement to 50 Mbar, but at that point also stiffens relative to the QMD fit. At very high pressure of 200 Mbar, the SESAME 2150 and the current EOS come into agreement, which is due to both using models that go to the same limit. The issue in the current EOS is that the thermal models are not correct in the interpolation to this limit, in such a way that we can not preserve accuracy at the very high and at the same time moderately high pressures. This will involve future work of developing new models.

Next in Fig. 9 isotherms of the EOS are compared with the QMD results for temperature up to 8 eV, and the Hugoniot path is shown by the dotted line up to 30 Mbar. Also we compare with the SESAME 2150 results, which are stiffening too much with temperature increase which results in the over stiff Hugoniot. The accurate modeling of this warm dense liquid regime is one of the main advancements of this work.

At lower temperatures, from 300 K to 17 000 K, we agree with the QMD results of Bouchet *et al.* [6] for the HPC and liquid phases and the melt curve up to 1500 GPa. The maximum difference is 3% at the highest pressure and lowest temperature, but generally less than 1% difference. For the gamma phase we compare with the preheated shock data of Chen and Ahrens [57]. Here iron is heated at ambient pressure to 1573 K and then shocked. Our EOS results are plotted

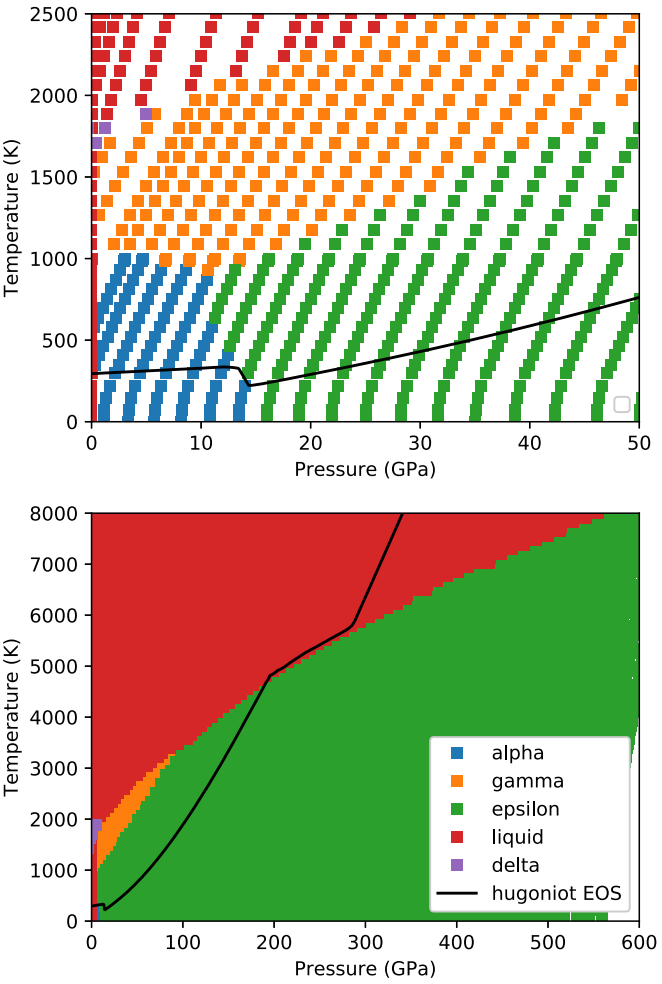

FIG. 11. Phase diagram for iron from the current EOS. The five phases including the liquid phase are shown along with the priciple Hugoniot, $\rho_0 = 7.874$ g/cm^3.

against the experiment in Fig. 10. Along with the isobaric thermal expansion this fixes our EOS for the gamma phase, which then yields an alpha-gamma-epsilon triple point at about 10.8 GPa and 890 K, as well as a gamma-epsilon-liquid triple point at about 100 GPa and 3400 K.

Lastly we consider the overall phase diagram for iron. As shown in Fig. 11, the room temperature alpha-epsilon transition occurs at 13 GPa, which is in agreement with the DAC data of Fig. 7. The principle shock Hugoniot passes through those two phases before beginning to melt at about 195 GPa and 4800 K, completion of melt is then at about 290 GPA and 5850 K. The gamma phase extends to a maximum pressure of 100 GPa. It has been speculated in the past that there exists a phase other than epsilon below the melt curve at higher pressures than this, but current theory [6] and experiment [58,59] do not support this and we have no such phase in our EOS. The epsilon phase has been shown through DFT studies to be the stable ground-state phase up to 7 TPa [60], where fcc, and at much higher pressure bct phases become the stable phase. We do not include these higher pressure phases in the EOS. Our melt curve is in good agreement with the results of Anzellini *et al.* [61] and the QMD results [6], including at 1500 GPa where we have a melt temperature of 12800 K.

IV. CONCLUSION

We have performed wide ranging quantum molecular dynamics calculations for the equation of state of warm dense iron. At temperature lower than 5 eV the Kohn-Sham method remains computationally tractable. A critical issue is the correct use of a pseudopotential with sufficiently small cutoff radius and inclusion of a sufficient number of valence electrons to properly account for compression as well as temperature ionization effects. We point out that the previous calculations of Wang *et al.* use an inappropriate pseudopotential and hence, their results are low in pressure densities above 16 g/cm^3. To achieve accurate results for temperatures up to 100 eV we have used a gradient corrected orbital-free density functional theory. This method relies on matching Kohn-Sham method results at sufficiently high temperature to determine the strength of the gradient correction. In total then our calculations cover fluid regime iron from 7 to 30 g/cm^3 and temperature from 1 to 100 eV. Finally, we calculated the Hugoniot to over 20 TPa, and found very good agreement with available experimental shock Hugoniot data, thus generally validating our QMD approach and calculations. In addition we have used the warm dense QMD data in conjunction with other recent low temperature QMD and experimental results to produce a new SESAME EOS for iron. This has highlighted some limitation in our ionic thermal model at very high pressures, but below 50 Mbar we provide an accurate representation of the liquid and solid phases.

ACKNOWLEDGMENTS

We thank S. Rudin and J. Wills for their calculations of the VASP and all-electron cold curves, as well as S. Mazevet for providing his solid-phase QMD results. This work was performed under the auspices of Los Alamos National Laboratory, which is operated by Los Alamos National Security, LLC, for the National Nuclear Security Administration of the US Department of Energy under Contract No. DE-AC52-06NA25396.

[1] A. Laio, S. Bernard, G. L. Chiarotti, S. Scandolo, and E. Tosatti, Science **287**, 1027 (2000).
[2] S. Seager, M. Kuchner, C. A. Hier-Majumder, and B. Militzer, Astrophys. J. **669**, 1279 (2007).
[3] M. Ćuk, S. T. Stewart, S. J. Lock, and D. Hamilton, Nature **539**, 402 (2016).
[4] J. M. Brown and R. G. McQueen, J. Geophys. Res. **91**, 7485 (1986).
[5] D. Batani, A. Morelli, M. Tomasini, A. Benuzzi-Mounaix, F. Philippe, M. Koenig, B. Marchet, I. Masclet, M. Rabec, C. Reverdin, R. Cauble, P. Celliers, G. Collins, L. Da Silva, T. Hall, M. Moret, B. Sacchi, P. Baclet, and B. Cathala, Phys. Rev. Lett. **88**, 235502 (2002).
[6] J. Bouchet, S. Mazevet, G. Morard, F. Guyot, and R. Musella, Phys. Rev. B **87**, 094102 (2013).
[7] C. Wang, Z.-B. Wang, Q.-F. Chen, and P. Zhang, Phys. Rev. E **89**, 023101 (2014).
[8] S. P. Lyon and J. D. Johnson, Los Alamos Technical Report, LA-UR-92-3407 (1992).
[9] G. I. Kerley, Sandia Report: Multiphase equation of state for iron, SAND93-0027 (1993).
[10] A. B. Medvedev, Combustion, Explosion, and Shock Waves **50**, 582 (2014).
[11] P. I. Dorogokupets, A. M. Dymshits, K. D. Litasov, and T. S. Sokolova1, Sci Rep. **7**, 41863 (2017).
[12] R. G. Parr and W. Yang, *Density-Functional Theory of Atoms and Molecules* (Oxford, UK, 1989), see Chap. 9.
[13] F. Lambert, J. Clérouin, and G. Zérah, Phys. Rev. E **73**, 016403 (2006).
[14] T. Sjostrom and S. Crockett, Phys. Rev. B **92**, 115104 (2015).
[15] P. Giannozzi *et al.*, J. Phys.: Condens. Matter **21**, 395502 (2009).
[16] J. P. Perdew, K. Burke, and M. Ernzerhof, Phys. Rev. Lett. **77**, 3865 (1996).
[17] P. E. Blöchl, Phys. Rev. B **50**, 17953 (1994).
[18] G. Kresse and D. Joubert, Phys. Rev. B **59**, 1758 (1999).
[19] J. M. Walsh, M. H. Rice, R. G. Mcqueen, and F. L. Yarger, Phys. Rev. **108**, 196 (1957).
[20] L. V. Al'tshuler, K. K. Krupnikov, B. N. Ledenev, V. I. Zhuchikhin, and M. I. Brazhnik, Zh. Eksp. Teor. Fiz. **34**, 874 (1958) [Sov. Phys.- JETP **7**, 606 (1958)].
[21] L. V. Al'tshuler, S. B. Kormer, A. A. Bakanova, and R. F. Trunin, Zh. Eksp. Teor. Fiz. **38**, 790 (1960) [Sov. Phys.- JETP **11**, 573 (1960)].
[22] L. V. Al'tshuler, S. B. Kormer, M. I. Brazhnik, L. A. Vladimirov, M. P. Speranskaya, and A. I. Funtikov, Zh. Eksp. Teor. Fiz. **38**, 1061 (1960) [Sov. Phys.- JETP **11**, 766 (1960)].
[23] R. G. McQueen and S. P. Marsh, J. Appl. Phys. **31**, 1253 (1960).
[24] L. V. Al'tshuler, A. A. Bakanova, and R. F. Trunin, Zh. Eksp. Teor. Fiz. **42**, 91 (1962) [Sov. Phys.- JETP **15**, 65 (1962)].

[25] I. C. Skidmore and E. Morris, *Thermodynamics of Nuclear Materials* (IAEA, Vienna, 1962), p. 173.
[26] K. K. Krupnikov, A. A. Bakanova, M. I. Brazhnik, and R. F. Trunin, Dokl. Akad. Nauk SSSR **148**, 1302 (1963) [Sov. Phys.-Dokl. **8**, 205 (1963)].
[27] A. S. Balchan and G. R. Cowan, J. Geophys. Res. **71**, 3577 (1966).
[28] L. V. Al'tshuler, B. N. Moiseev, L. V. Popov, G. V. Simakov, and R. F. Trunin, Zh. Eksp. Teor. Fiz. **54**, 785 (1968) [Sov. Phys.-JETP **27**, 420 (1968)].
[29] R. G. McQueen, S. P. Marsh, J. W. Taylor, J. N. Fritz, and W. J. Carter, The equation of state of solids from shock wave studies, In *High Velocity Impact Phenomena*, edited by R. Kinslow (Academic Press, New York, 1970), pp. 293–417; appendices pp. 515–568.
[30] R. F. Trunin, M. A. Podurets, G. V. Simakov, L. V. Popov, and B. N. Moiseev, Zh. Eksp. Teor. Fiz. **62**, 1043 (1972) [Sov. Phys.-JETP **35**, 550 (1972)].
[31] L. V. Al'tshuler and B. S. Chekin, Metrology of high pulsed pressures, in *Proceedings of the 1st All-Union Pulsed Pressures Symposium* (VNIIFTRI, Moscow, 1974), vol. 1, pp. 5–22 [in Russian].
[32] L. V. Al'tshuler, N. N. Kalitkin, L. V. Kuz'mina, and B. S. Chekin, Zh. Eksp. Teor. Fiz. **72**, 317 (1977) [Sov. Phys.- JETP **45**, 167 (1977)].
[33] S. P. Marsh (Ed.), *LASL Shock Hugoniot Data* (University of California Press, Berkeley, 1980).
[34] L. V. Al'tshuler, A. A. Bakanova, I. P. Dudoladov, E. A. Dynin, R. F. Trunin, and B. S. Chekin, Zh. Prikl. Mekh. Tekhn. Fiz. **2**, 3 (1981) [J. Appl. Mech. Techn. Phys. **22**, 145 (1981)].
[35] C. E. Ragan, Phys. Rev. Ser. A **29**, 1391 (1984).
[36] R. S. Hixson and J. N. Fritz, Shock compression of iron, in *Shock Compression of Condensed Matter*, edited by S. C. Schmidt, R. D. Dick, and D. G. Tasker (North Holland, Amsterdam, 1992), pp. 69–72.
[37] R. F. Trunin, M. A. Podurets, L. V. Popov, V. N. Zubarev, A. A. Bakanova, V. M. Ktitorov, A. G. Sevast'yanov, G. V. Simakov, and I. P. Dudoladov, Zh. Eksp. Teor. Fiz. **102**, 1433 (1992) [Sov. Phys. JETP **75**, 777 (1992)].
[38] R. F. Trunin, M. A. Podurets, B. N. Moiseev, G. V. Simakov, and A. G. Sevast'yanov, Zh. Eksp. Teor. Fiz. **103**, 2189 (1993) [Sov. Phys. JETP **76**, 1095 (1993)].
[39] R. F. Trunin, Usp. Fiz. Nauk **164**, 1215 (1994) [in Russian].
[40] L. V. Al'tshuler, R. F. Trunin, K. K. Krupnikov, and N. V. Panov, Usp. Fiz. Nauk **166**, 575 (1996) [Phys. Usp. **39**, 539 (1996)].
[41] J. M. Brown, J. N. Fritz, and R. S. Hixson, J. Appl. Phys. **88**, 5496 (2000).
[42] M. D. Knudson and M. P. Desjarlais, Phys. Rev. B **88**, 184107 (2013).
[43] G. I. Kerley, Los Alamos Technical Report, LA-08833-M (1981).
[44] R. P. Feynman, N. Metroplis, and E. Teller, Phys. Rev. **75**, 1561 (1949).
[45] E. Chisolm, Los Alamos Technical Report, LA-UR-05-2297 (2003).
[46] J. C. Boettger and D. C. Wallace, Phys. Rev. B **55**, 2840 (1997).
[47] D. J. Andrews, J. Phys. Chem. Solids **34**, 825 (1973).
[48] G. De Lorenzi-Venneri and S. D. Crockett, AIP Conf. Proc. **1793**, 050020 (2017).
[49] R. Kohlhaas and M. Braun, Archiv Fur Das Eisenhuttenwesen **34**, 391 (1963).
[50] P. D. Desai, J. Phys. Chem. Ref. Data **15**, 967 (1986).
[51] J. D. Johnson, High Pressure Res. **6**, 277 (1991).
[52] CINDAS Recommended Data Based on CINDAS Evaluation from Available Information. Retrieved from CINDAS LLC Thermophysical Properties of Matter Database (TPMD). Version 10.0 at http://cindasdata.com/
[53] M. J. Assael, K. Kakosimos, R. M. Banish, J. Brillo, I. Egry, R. Brooks, P. N. Quested, K. C. Mills, A. Nagashima, Y. Sato, and W. A. Wakeham, J. Phys. Chem. Ref. Data **35**, 285 (2006).
[54] H. K. Mao, Y. Wu, L. C. Chen, and J. F. Shu, J. Geophys. Res. **95**, 21737 (1990).
[55] S. Ono, T. Kikegawa, N. Hirao, and K. Mibe, Am. Mineral. **95**, 880 (2010).
[56] A. Dewaele, P. Loubeyre, F. Occelli, M. Mezouar, P. I. Dorogokupets, and M. Torrent, Phys. Rev. Lett. **97**, 215504 (2006).
[57] G. Q. Chen and T. J. Ahrens, Mat. Res. Soc. Symp. Proc. **499**, 41 (1998).
[58] J. H. Nguyen and N. C. Holmes, Nature **427**, 339 (2004).
[59] A. Denoeud, N. Ozaki, A. Benuzzi-Mounaix, H. Uranishi, Y. Kondo, R. Kodama, E. Brambrink, A. Ravasio, M. Bocoum, J.-M. Boudenne, M. Harmand, F. Guyot, S. Mazevet, D. Riley, M. Makita, T. Sano, Y. Sakawa, Y. Inubushi, G. Gregori, M. Koenig, and G. Morarde, Proc. Natl. Acad. Sci. USA **113**, 7745 (2016).
[60] C. J. Pickard and R. J. Needs, J. Phys.: Condens. Matter **21**, 452205 (2009).
[61] S. Anzellini, A. Dewaele, M. Mezouar, P. Loubeyre, and G. Morard, Science **340**, 464 (2013).